

Analysis of FORTE Data to Extract Ionospheric Parameters

Robert A. Roussel-Dupré¹, Abram R. Jacobson², and Laurie A. Triplett¹

*¹Atmospheric and Climate Sciences Group, MS F659, Los Alamos National Laboratory, Los Alamos, NM
87545*

*²Space and Atmospheric Sciences Group, MS D466, Los Alamos National Laboratory, Los Alamos, NM
87545*

Abstract

The ionospheric transfer function is derived for a spherically symmetric ionosphere with an arbitrary radial electron density profile in the limit where the radio frequencies of interest () are much larger than the plasma frequency (ω_{pe}). An expansion of the transfer function to second order in the parameter $X (= \omega_{pe}^2 / \omega^2)$ is carried out. In this limit the dispersive properties of the ionosphere are manifested as a frequency dependent time of arrival that includes quadratic, cubic, and quartic terms in $1/\omega$. The coefficients of these terms are related to the TEC (total electron content) along the slant path from transmitter to receiver, the product of TEC and the longitudinal magnetic field strength along the slant path, and refractive bending and higher order electron density profile effects, respectively. By fitting the time of arrival vs frequency of a transionospheric signal to a polynomial in $1/\omega$, it is possible to extract the TEC, the longitudinal magnetic field strength, the peak electron density, and an effective thickness for the ionosphere. This exercise was carried out for a number of transionospheric pulses measured in the VHF by the FORTE satellite receiver and generated by the Los Alamos Portable Pulser. The results are compared with predictions derived from the International Reference Ionosphere and the United States Geological Survey geomagnetic field model.

1. INTRODUCTION

The role of the ionosphere in disrupting radio wave transmission and the information carried by these waves continues to be a topic of considerable interest. Activity in this area has been spurred on by technological advances made in communications, navigation, surveillance, remote sensing, radar technology, ionospheric sounding, ionospheric modifications, and the deployment of space-based detectors and transmitters. The implementation, in turn, of more sophisticated technologies has necessitated a more detailed investigation into the effects of the ionosphere on radio wave propagation and into the detailed characteristics of the ionospheric channel. A recent example that delineates the importance of understanding ionospheric effects comes from satellite broadband measurements of lightning generated pulses at very high frequencies (VHF) by FORTE and Blackbeard (*Jacobson et al.*, 2000; *Jacobson et al.*, 1999; *Holden, Munson, and Devenport*, 1995; *Massey and Holden*, 1995). Extraction of ionospheric dispersion and higher order effects is now routinely performed prior to the determination of the properties and statistics of the lightning pulses. It can be generally stated on the basis of these studies and others that the detection, accurate geolocation, and interpretation of transient electromagnetic signals from space requires a detailed understanding of the distortions introduced by the intervening ionospheric plasma. Indeed, the magnitude of phase and amplitude changes imparted to an electromagnetic wave that propagates through the ionosphere depends strongly on frequency, and the superposition of such effects over a broad frequency range and over large distances can result in significant distortion of the signal and obscuration of the source characteristics.

The converse is also true however, i.e., if the source is well characterized then it is possible to garner information about the ionosphere from the transionospheric signal. Most experimental studies of the ionospheric plasma (cf, *Kelley*, 1989; *Rishbeth and Garriott*, 1969; for a general review of this subject) have relied on ground-based bottomside and satellite-based topside ionosondes, incoherent scatter radar measurements, space-based radio beacon experiments at VHF, UHF, and S-band, and *in situ* rocket measurements of the plasma density. Many aspects of the steady-state ionospheric density profile and its dynamic evolution have been deduced from synoptic measurements obtained over many decades, and a tremendous body of literature exists on the subject. The ionosphere, however, is a complex medium subject to diurnal, seasonal and long-term variations driven primarily by solar activity but also by local disturbances, the neutral wind and unstable plasma configurations. Even the most detailed ionospheric models have not been very successful in predicting the characteristics of any given propagation channel for extended periods of time (exceeding tens of minutes to hours), and significant research remains to be performed before adequate models are developed.

In this paper we examine the possibility of exploiting broadband signals launched from the ground and detected by satellite receivers to extract information about the Earth's ionosphere. In Section 2, we derive the ionospheric transfer function for a spherically symmetric ionosphere with an arbitrary radial electron density profile in the limit where the radio frequencies of interest () are much larger than the plasma frequency (ω_{pe}). In Section 3, we describe the FORTE data and the analysis used to extract information about the ionosphere. In Section 4, we compare the results of our analysis to predictions derived from the International Reference Ionosphere and the

United States Geological Survey geomagnetic field model. Conclusions are drawn in Section 5.

2. IONOSPHERIC TRANSFER FUNCTION

Most of the formalism presented in this section can be found in various texts on the subject of ionospheric radio wave propagation (e.g., *Budden*, 1985, and *Davies*, 1965). The basic theoretical analysis that leads us to a new expression for the ionospheric transfer function is repeated here for completeness. Modeling of the propagation of an electromagnetic pulse (such as that produced by a lightning discharge) through the ionosphere requires that we solve the vector wave equation for the electric field; namely,

$$\frac{\partial^2 \underline{E}}{\partial t^2} - c^2 \nabla^2 \underline{E} + c^2 (\nabla \cdot \underline{E}) = -4 \frac{\underline{J}}{t}, \quad (1)$$

where \underline{E} is the wave electric field vector and \underline{J} is the ionospheric plasma current density. Substituting for the plasma current density obtained from collisionless, magnetoionic theory (cf., *Davies*, 1965) and taking the temporal Fourier transform of Eq. (1) yields an equation of the form,

$$-\frac{\omega^2}{c^2} \underline{\epsilon} \cdot \underline{\tilde{E}} - \nabla^2 \underline{\tilde{E}} + (\nabla \cdot \underline{\tilde{E}}) = 0, \quad (2)$$

where $\underline{\epsilon}$ is the dielectric tensor of the ionospheric plasma,

$$= \begin{pmatrix} 1 & i & 0 \\ -i & 2 & 0 \\ 0 & 0 & 3 \end{pmatrix}, \quad (3)$$

$$\text{with } \epsilon_1 = 1 + \frac{4}{\omega_p^2}, \quad \epsilon_2 = \frac{4}{\omega_H^2}, \quad \epsilon_3 = 1 + \frac{4}{\omega_{pe}^2}, \quad \epsilon_p = \frac{i}{4} \frac{X}{(1 - Y_e^2)},$$

$$\epsilon_H = \frac{-i}{4} \frac{XY_e}{(1 - Y_e^2)}, \quad \epsilon_{//} = \frac{i}{4} \frac{X}{\omega_{pe}^2}, \quad X = \frac{\omega^2}{\omega_{pe}^2}, \quad Y_e = \frac{\omega_{ce}}{\omega}, \quad Y_{\perp} = Y_e \sin(\theta), \quad Y_L =$$

$Y_e \cos(\theta)$, ω is the angular frequency of the incident wave, ω_{pe} is the plasma frequency,

ω_{ce} is the electron cyclotron frequency, θ is the angle between the wave vector \underline{k} and the

background magnetic field \underline{B}_0 , and $\tilde{\underline{E}}$ is the temporal Fourier transform of the electric field vector. Substituting an expression for the electric field vector of the form,

$$\tilde{\underline{E}}(\underline{r}, \omega) = \underline{e}(\underline{r}, \omega) \exp(i \underline{k} \cdot \underline{dr}), \quad (4)$$

into Eq. (2) yields, in the limit of geometrical optics,

$$-\frac{\omega^2}{c^2} \underline{e} + k^2 \underline{e} - \underline{k} (\underline{k} \cdot \underline{e}) = 0. \quad (5)$$

Equation (5) forms the basis for nearly all studies of radio wave propagation through a deterministic ionosphere. The general solution to this equation yields the well-known Appleton-Hartree dispersion relation, which identifies two normal modes (ordinary and extraordinary) that differ in their polarization relative to the geomagnetic field and in their dispersion relations. The collisionless form of the Appleton-Hartree dispersion relation is written,

$$\mu_{\text{O}}^2 = 1 - \frac{2X(l-X)}{2(l-X) - Y_{\text{T}}^2 \pm \sqrt{Y_{\text{T}}^4 + 4(l-X)^2 Y_{\text{L}}^2}} \quad (6)$$

where μ ($= ck/$) is the plasma index of refraction, and all other symbols have been defined previously. The plus (minus) sign in Eq. (6) corresponds to the ordinary (extraordinary) or O (E) mode as defined in ionospheric physics (cf., Rishbeth and Garriott, 1969).

In the limit $Y_{\text{T}}^4 / 4 \ll (l-X)^2 Y_{\text{L}}^2$ (referred to as the quasi-longitudinal approximation), this equation further simplifies to,

$$\mu_{\text{O}}^2 = 1 - \frac{X}{1 \pm Y_{\text{L}}} \quad (7)$$

Assuming that Y_{L} is small, the group velocity can be written,

$$V_g^O = c \sqrt{1 - \frac{X}{1 \pm Y_L}} \quad (8)$$

As is evident from Eq. (8), the net effect of dispersion is to introduce a time delay in the arrival of a particular frequency component of the incident pulse at a specified detector such that the high frequencies arrive first. This effect will be illustrated below for a specific example.

The eigenvectors for the ordinary and extraordinary modes correspond to right-hand and left-hand circularly polarized waves in the Northern Hemisphere. In a coordinate system with the wave vector \underline{k} in the z-direction and the geomagnetic field B_0 at an angle to the z-direction and in the z-y plane, the eigenvectors are given by,

$$\underline{e}_E^O(r, \omega) = \begin{pmatrix} E_E^O(r, \omega) \\ \pm i \\ 0 \end{pmatrix}, \quad (9)$$

where $E_E^O(r, \omega)$ is the Fourier transform of the x-component of the ordinary (right-hand, +i) and extraordinary (left-hand, -i) circularly polarized wave-components launched by the transmitter. Note that any polarization can be represented as the superposition of right- and left-circularly polarized waves and that Eq. (9) is valid provided both the transmitter and the receiver are located outside the ionospheric plasma.

According to Eqs. (4) and (9) the transionospheric signal can be written as the convolution (product) of the transmitted signal and the ionospheric impulse response (transfer function) in the time (frequency) domain. Thus, the ionosphere can be treated as a filter that to zeroth order is both dispersive and birefringent (separates wave polarization into two normal modes) and the transfer function is given by the exponential term in Eq. (4).

In the limit that the plasma frequency is much smaller than the wave frequency (i.e., $X \ll 1$), a condition that is satisfied over most of the VHF bandwidth of interest to our analysis of FORTE data, it is possible to further simplify the phase integral in the deterministic transfer function. For a spherically symmetric ionosphere with a radially varying electron density profile, the phase integral to second order in the variable $X = \omega_{pe}^2 / \omega^2$ is given by,

$$\begin{aligned}
\int_0^r \frac{\mathbf{k}_{O_E} \cdot d\mathbf{r}}{c} &= \frac{O_E}{c} S_0 \\
&- \frac{R_s}{c} \frac{A_{O_E} X}{R_E} \frac{r dr}{\sqrt{r^2 - R_E^2 \sin^2}} \\
&- \frac{R_s}{c} \frac{X^2}{R_E} \frac{B_{O_E}}{4} + \frac{A_{O_E}^2}{2} \frac{r dr}{\sqrt{r^2 - R_E^2 \sin^2}} \\
&- \frac{R_s}{c} \frac{A_{O_E}^2 X^2}{R_E} \frac{R_E^2 \sin^2}{r^2 - R_E^2 \sin^2} \frac{r dr}{3/2} \\
&+ \frac{R_s}{c} \frac{A_{O_E} X}{R_E} \frac{r dr}{r^2 - R_E^2 \sin^2} \frac{3/2}{\sqrt{1 - \frac{R_E^2}{R_s^2} \sin^2}} \frac{R_E^3 \sin^2 \cos}{8 \frac{S_0}{R_s}}
\end{aligned}
\tag{10}$$

where subscripts (O, E) refer to the ordinary and extraordinary modes, R_E is the earth's radius, R_s is the geocentric radial distance to the receiver, S_0 is the slant path distance from the transmitter to the receiver, θ is the angle between local zenith and the receiver location, and the parameters A_{O_E} and B_{O_E} are defined as,

$$A_{\text{O}_\text{E}} = \frac{1}{1 - \frac{1}{2} Y_{\text{T}}^2 \pm \sqrt{\frac{Y_{\text{T}}^4}{4} + Y_{\text{L}}^2}} \quad (11)$$

$$B_{\text{O}_\text{E}} = A_{\text{O}_\text{E}}^2 Y_{\text{T}}^2 \mp \sqrt{Y_{\text{T}}^4 + 4 Y_{\text{L}}^2} \pm \frac{4 Y_{\text{L}}^2}{\sqrt{Y_{\text{T}}^4 + 4 Y_{\text{L}}^2}}$$

with Y_{T} and Y_{L} defined previously and the upper (lower) sign associated with the ordinary (extraordinary) mode. This result was derived with the added constraint that the transmitted wave must arrive at the receiver. Because the ray-path is in general frequency-dependent the latter constraint has the effect of introducing a frequency-dependent launch angle. This effect is incorporated in Eq. (10) and can also lead to a frequency dependent polarization that would modify the source spectrum as measured by the receiver.

The first term in Eq. (10) corresponds to the vacuum accumulated phase change along the slant path between the transmitter and receiver. The second through fifth terms represent the corrections introduced by the ionosphere. In the limit that Y_{T} and Y_{L} are small (again an excellent approximation for most of the VHF bandwidth of interest) A_{O_E}

$1 \mp Y_{\text{L}}$ and the second term of Eq. (10) reduces to the sum of two terms, one proportional to the integrated electron density (total electron content or TEC) along the slant path and the other proportional to the integrated product of the electron density and Y_{L} along the slant path. The third term in Eq. (10) incorporates ionospheric corrections associated with higher order integral moments of the electron density while the fourth

and fifth terms represent corrections resulting from refractive bending. Note that the latter effects are second order in the parameter X ; however, this term becomes large as X approaches $\pi/2$.

For some applications such as geolocation of the source, it is necessary to obtain the arrival time of the signal at the receiver. The frequency dependent time delay, τ_E^O is given by,

$$\begin{aligned}
& \frac{A_O}{R_E} = \frac{1}{c} S_0 \\
& + \frac{1}{c} \frac{R_s}{R_E} \frac{X}{2} A_{O_E} - \frac{d A_{O_E}}{d} \frac{r dr}{\sqrt{r^2 - R_E^2 \sin^2}} \\
& + \frac{1}{c} \frac{R_s}{R_E} \frac{X^2}{4} 3 B_{O_E} + \frac{A_{O_E}^2}{2} - \frac{d}{d} B_{O_E} + \frac{A_{O_E}^2}{2} \frac{r dr}{\sqrt{r^2 - R_E^2 \sin^2}} \\
& + \frac{1}{c} \frac{3}{8} \frac{R_s}{R_E} A_{O_E}^2 - \frac{d A_{O_E}^2}{d} X^2 \frac{R_E^2 \sin^2}{r^2 - R_E^2 \sin^2} \frac{r dr}{3/2} \\
& + \frac{1}{c} \frac{3}{4} \frac{R_s}{R_E} A_{O_E} X \frac{r dr}{r^2 - R_E^2 \sin^2} \frac{3/2}{3/2} \frac{R_s}{R_E} A_{O_E} - \frac{d A_{O_E}}{d} \\
& \cdot X \frac{r dr}{r^2 - R_E^2 \sin^2} \frac{3/2}{3/2} \frac{\sqrt{1 - \frac{R_E^2}{R_s^2} \sin^2} R_E^3 \sin^2 \cos}{\frac{S_0}{R_s}}
\end{aligned}$$

(12)

It can be noted from equations (12) that the chirp introduced by the ionospheric filter is to first order inversely proportional to frequency squared. For impulsive signals whose

duration is small compared to the ionospheric dispersion, this chirp can be measured across a given bandwidth or with narrow-band receivers at several frequencies and can be removed to obtain the vacuum line-of-sight delay.

The analysis described in this section forms the basis for studying many of the important collisionless effects associated with transionospheric radio wave propagation. The results can be used to calculate transionospheric signals under various ionospheric conditions and as such provide the foundation for development of a useful predictive capability.

To illustrate the manner in which the transionospheric signal can be determined from the results provided above, we apply our analysis to a simple case in which the transmitted signal is a dirac delta function in time and we only consider the second term in the expansion of the ionospheric transfer function in the quasi-longitudinal approximation. In general, the transionospheric signal in the time domain can be written

$$\underline{E}_{TI}(t) = \frac{1}{2} \int_{-\infty}^{\infty} \underline{e}(r, \omega) H_I(\omega) e^{i\omega t} d\omega \quad (13)$$

where H_I is the ionospheric transfer function which can be derived from the results obtained above. In the limit that the quasi-longitudinal approximation applies and when $X \ll 1$, the transfer function for the deterministic ionosphere can be written

$$H_I(\omega) = \frac{1}{2} \exp \left[\frac{i\omega^2}{\pm \omega_{ce} \cos \theta} \right] + \exp \left[\frac{-i\omega^2}{- \pm \omega_{ce} \cos \theta} \right] \quad (14)$$

where f_{TEC} (in MHz) = $8.430 \times 10^4 \text{ TEC}$, TEC is the total electron content along the propagation path in units of 10^{17} m^{-2} , all frequencies are expressed in MHz, the + (-) corresponds to the ordinary (extraordinary) mode, and where we have omitted the effects of refractive bending and assumed a density weighted gyrofrequency (f_{ce}) and angle (θ) between the propagation vector and the magnetic field.

Usually the deterministic ionosphere is well represented by the transfer function Eq. (14) for frequencies above 20-30 MHz. In this case the ionosphere is characterized in terms of its TEC and an average value for the product of f_{ce} and $\cos \theta$ (or longitudinal component of the gyrofrequency). However, at frequencies approaching the peak plasma frequency (typically 3-15 MHz) and in cases of oblique incidence at frequencies as high as 40 MHz, it is necessary to include higher-order terms in the expansion about small X and to incorporate refractive bending. In addition, Earth curvature effects must be incorporated in order to model the refractive bending accurately. These latter effects are included in the form of the phase correction and time delay derived here and given by Eq. (10) and Eq. (12), respectively. We note that at sufficiently small elevation angles and high plasma frequencies, the expansion in terms of X breaks down and it is necessary to employ the full form of the Appleton-Hartree dispersion relation in the exponent of Eq. (4). An equivalent alternative would be to perform a 3-D ray-tracing calculation for each frequency.

The impulse response function for a deterministic ionosphere is obtained from Eqs. (13)-(14) assuming that the transmitted signal is a unit impulse whose Fourier transform is given by $\underline{e}(\underline{r}, \omega) = E_0 \delta(\omega - \omega_0) e^{i \omega_0 t_0}$ where t_0 is the time at which the pulse is

launched and E_0 , t are normalization constants. Note that the transmitted signal is linearly polarized and is therefore composed of an equal mix of ordinary and extraordinary modes. The net result is given by

$$E_{TI} = E_0 \exp\left[-\frac{2}{x} J_1(x)\right] \cos\left[\omega_{ce} \cos\left(\frac{x}{2}\right) (t - t_0)\right], \quad (15)$$

where J_1 is a first order Bessel function, the argument $x = 2 \sqrt{\omega_{ce}} (t - t_0)^{1/2}$, and here ω_{ce} is in radians / s ($= 5.30 \times 10^{11}$ TEC with TEC in units of 10^{17} m^{-2}). Plots of E_{TI} and its spectrogram for a TEC = 1, $f_{ce} = 0.8$ MHz, $\theta = 20^\circ$, and $t_0 = 1 \mu\text{s}$ are provided in Figs. 1(a) and 1(b). Note that the initial Dirac impulse becomes stretched out in time over tens of microseconds by the ionosphere and that the ionosphere produces a frequency-dependent group delay such that the high-frequency components of the impulse arrive first. The beating of the two modes can be seen in both the temporal plot [Fig. 1(a)] and the spectrogram [Fig. 1(b)]. One obvious effect of dispersion is to lower the amplitude of the low-frequency components in the time domain relative to that of the high frequencies. We can now proceed to analyze the FORTE data in the context of this theoretical framework.

3. FORTE BROADBAND DATA

The FORTE satellite has performed continuous observations of lightning since its launch on 29 August 1997. FORTE is in a 70° inclination, circular low-Earth orbit.

FORTE captures and stores discrete records of very-high-frequency (VHF) radio-wave signals. The radio receiver comprises two 50-Megasample-per-second passbands, each analog-filtered to 22-MHz bandwidth. In the data to follow, we typically run with at least one 22-MHz channel placed in the range 26-48 MHz, with a nominal 38-MHz center ("lo band"), and the other in the range 118 - 140 MHz, with a nominal 130-MHz center ("hi-band"). The performance of the FORTE rf payload, plus some of the initial characteristics of the lightning observations, have been described in detail elsewhere [Jacobson *et al.*, 2000; Jacobson *et al.*, 1999].

The FORTE receiver is triggered by a multichannel coincidence trigger system. Each 1-MHz trigger subband (eight in each 22-MHz-wide channel; sixteen total) has a noise-compensation option, so that the trigger threshold is set in either absolute level or as db *above a low-pass-filtered noise level* in that 1-MHz subband, i.e. as a "noise-riding threshold". In this way the trigger system can in practice trigger on lightning signatures that would otherwise be overwhelmed by anthropogenic radio carriers appearing in the overall analog passband. In the data used here, we use noise-riding-threshold triggering and require five (out of eight) 1-MHz subbands to trigger in coincidence (with a coincidence window adequate to compensate for ionospheric dispersion, namely 162 μ s). We typically require the signal to rise at least 14 - 20 dB (depending on the program and the intended class of lightning signals) above the noise background in each 1-MHz subband contributor to the "5-out-of-8" OR.

Each 22-MHz channel is connected to a different linear polarization of a two-polarization log-periodic antenna. The antenna is mounted on a boom facing the satellite nadir, usually within a few degrees. The antenna is designed to place an approximate

minimum (throughout the VHF spectrum) on the limb of the Earth as seen from FORTE, and a lobe maximum at nadir. (From orbital altitude, the limb is located on a “small circle” of arc-diameter 6,400 km.)

The data used in this paper are FORTE receptions of signals emanating from the Los Alamos Portable Pulser, a broadband VHF/UHF single-pulse transmitter at Los Alamos, New Mexico (35.87 deg N, -106.33 deg E) [Massey *et al.*, 1998]. Although the transmitted signal is linearly polarized, at the satellite the signal is the sum of a "fast" and a delayed "slow" mode, due to ionospheric birefringence imposed by the geomagnetic field (see discussion in the previous section).

The first step in processing FORTE data from LAPP illuminations is to produce a spectrogram, that is, a sliding-window Fourier transform. The second step is that this spectrogram is then filtered with a view to suppressing CW interference carriers. The filter procedure is just to suppress rows of the spectrogram in proportion to the inverse of the power in that row. The third step is roughly to fit a slant total electron content (TEC) which approximately accounts for the ionospheric dispersion proportional to f^{-2} ; details are given elsewhere [Jacobson *et al.*, 1999]. This TEC is used to dechirp the spectrogram by appropriately advancing rows (toward earlier times) just so as to compensate for the ionospheric dispersion proportional to f^{-2} .

Figure 2(a) shows the logarithm of the carrier-suppressed dechirped spectrogram for part of the low band, while Figure 2(b) shows the corresponding simultaneous spectrogram for the entirety of the high band, after carrier suppression. The color scale extends over 70 dB of total range. The dispersion removal has used a value of $8.54 \times 10^{17} \text{ m}^{-2}$ for the slant total electron content. The high band (Figure 2(b)) shows a single

pulse, while the low band (Figure 2(a)) shows a pair of pulses, due to the ionospheric birefringence. (The superimposed symbols and curves will be explained below.)

Inspection of the "fast"- and "slow"-mode pulses in the low-band spectrogram (Figure 2(a)) shows that, despite the correction for dispersion proportional to f^{-2} , *there is still residual curvature of the pulse signature*. Part of this curvature is due to the fast/slow splitting, but part is *due to the presence of a quartic term that is unrelated to birefringence*.

Our goal in this paper is to recover measurements of the true slant electron content, plus the quartic effect, in such a manner that these results not be biased or corrupted by the birefringence. Our approach is to find the median low-band signal, which is to say, the curve of frequency versus time that is the median (in time) of the two birefringent modes. This guarantees (see Eqs. 11-12) that there will be no bias from birefringence in a coordinated fit of the true slant TEC and the quartic term. The black asterisks are marked on the low-band (fast and slow modes) and high-band signals in Figure 2(a) and 2(b). These were placed by eye with a cursor. The faint curves through the low-band cursor points are polynomial fits to those two sets of points. The heavier curve is the desired median, halfway (in time) between the two faint curves.

Figure 2(c) shows the low-band median curve (as 40 black triangles) and the high-band cursor points (as 10 black triangles). The data and fitted points in Figure 2(c) are already dechirped in the same manner as are the spectrograms [Figures 2(a) and 2(b)]. This is to compress the display in time as much as possible, so as to highlight the residual quartic effects. The blue squares are a coordinated fit of true slant TEC and the quartic effect, *using only the 40 low-band median points*. The red squares are also a coordinated

fit of true slant TEC and the quartic effect, *but using both the 40 low-band median points and the high-band cursor points*. The red points are fit with a true slant TEC of $5.31 \times 10^{17} \text{ m}^{-2}$ coordinated with a quartic delay at 100 MHz of $0.43 \text{ } \mu\text{s}$. The blue points, ignoring the upper band, give a true slant TEC of $4.18 \times 10^{17} \text{ m}^{-2}$ coordinated with a quartic delay at 100 MHz of $0.53 \text{ } \mu\text{s}$. However, the blue points' failure to come close to the high-band data indicates that the low-band-only fit is incapable of resolving the quartic effect as well as is the two-band fit.

A similar analysis was repeated for all the LAPP data collected by FORTE under conditions when FORTE channels were tuned to cover both 26-51 MHz and 118-143 MHz bands simultaneously. All the coordinated fits of slant TEC and the quartic effect are with both frequency bands [like the red points in Figure 2(c)].

4. COMPARISON OF FORTE DATA WITH MODEL PREDICTIONS

The International Reference Ionosphere (IRI) code (cf, *Rawer and Bradley*, 1987; *Belitza*, 1990; *Belitza et al.*, 1993) is a useful tool for predicting the electron density, electron temperature, ion temperature, and ion composition of the ionosphere from 50 km to 2000 km altitude anywhere on the globe. The code is available through the National Space Science Data Center (NSSDC) and sponsored by the Committee on Space Research (COSPAR) and the International Union of Radio Science (URSI). IRI is updated depending on committee recommendations every year and the most recent version IRI-95 obtained in 1998 is used in our analysis. IRI generates electron density profiles by interpolating a series of tables developed from synoptic measurements

obtained with ionosondes, topside sounders, incoherent scatter radars and *in situ* rocket and satellite measurements. The database in some cases constitutes more than 20 years of measurements taken on an hourly basis.

Although IRI contains a magnetic field model, we decided to use a more recent and complete prescription developed by the National Geomagnetic Information Center (NGIC) of the United States Geological Survey (USGS; cf., *Quinn et al.*, 1995). The GEOMAG code computes the declination, inclination, total intensity, and grid variation of the Earth's magnetic field in geodetic coordinates from the coefficients of current and historical, global and regional, spherical harmonic models. We used the most recent version of the code that incorporates epochs 1990, 1995, and 2000.

We have developed a code called ITF (Ionospheric Transfer Function) at Los Alamos to compute the transfer function for the ionosphere as defined by Eqs. (4), (10), and (11). The integrals in Eq. (10) are performed along the slant path from a specified transmitter to a specified receiver, given the electron density and geomagnetic field vector along the path as provided by IRI and GEOMAG, respectively. In addition to the transfer function, ITF also calculates polarization information and the time delay as a function of frequency given by Eq. (12). A separate code, also developed at Los Alamos, named TIPC (for TransIonospheric Propagation Code) convolves the impulse response of the ionosphere against a given source pulse to yield the transionospheric signal. We carried out this exercise for two cases in which the source pulse was fixed and the ionospheric conditions were varied and passed the resulting signal through the FORTE pulse-analysis algorithms in order to check the accuracy of those calculations. In each case we performed two separate tests in which the quartic term was either included or

excluded from the ionospheric transfer function. Two 22 MHz bands centered at 38 MHz and 130 MHz were analyzed in all cases. When the quartic term was included the difference between the TEC deduced by the FORTE algorithm and the actual value generated by IRI/ITF was within $\sim 1\%$. The FORTE analysis in this case also yielded a quartic time delay at 100 MHz that was within 5 % of the value generated by ITF. When the quartic term was excluded from the transfer function, the FORTE algorithm yielded a TEC within $\sim 1\%$ of the ITF generated value and computed a very small quartic time delay at 100 MHz with a value for example around several ns when the generated value (when quartic term was included) was approximately 100 ns for the ionospheric conditions under consideration. Similar agreement was obtained for the electron-density-weighted product of the geomagnetic field and the cosine of the angle between the field and the Poynting vector (called the longitudinal magnetic field component). In both cases the computed values were within 5 % of the generated ones. These results gave us confidence that the particular FORTE algorithm used in this study can extract ionospheric parameters to a precision of less than 5 %.

In addition to deducing the TEC and the longitudinal magnetic field component from measurements of the frequency dependent time delay in the manner outlined in the previous section, it is also possible to derive the peak electron density and thickness of the ionosphere from the quartic term. To do so we must examine the quartic term in Eq. (12) in more detail and make some simplifying assumptions. First, we assume that the ionosphere can be represented by a curved slab with a constant radial electron density (N_{ep}) and a finite thickness (T). In this limit and taking the ratio of the refractive bending terms (ϵ_{bend}) to the TEC quadratic term (ϵ_{TEC}) we have,

$$\frac{\tau_{bend}}{\tau_{TEC}} = \frac{3}{4} \frac{\omega_{pe}^2}{\omega^2} \left(1 + \frac{R_s - R_E - T}{R_s - R_E} \frac{1}{\tan^2 \alpha} \right), \quad (16)$$

where ω_{pe} is the plasma frequency of the ionosphere and all other symbols have been defined previously. Given several measurements for various zenith angles of a broadband pulse and fitting the ratio of quartic to quadratic time delay (after removal of magnetic field effects) at a fixed frequency to the functional form given by Eq. (16), it is possible to determine the electron density. An effective slant thickness for the ionosphere is obtained by taking the ratio of the slant TEC to the computed peak electron density.

This analysis was performed for three occasions on which a LAPP pulse was detected by the FORTE satellite once every minute as the satellite passed from one pulser horizon to another. A listing of the UT month/day/year/time-of-day, the satellite elevation-angle as seen from the LAPP, and the geographic coordinates and altitude of the satellite for each of the FORTE collects is provided in Tables 1(a) – 1(c). In Figures 3(a)-3(e) we present for Case 1, the TEC, quartic time delay at 100 MHz, peak electron density, thickness, and the longitudinal component of the electron gyrofrequency in MHz as determined from the data using the analysis discussed in the previous section. The corresponding values obtained from the ITF code are also provided in Figures 3(a)-3(e) for comparison. Similar results were also generated for Cases 2 and 3 and are shown in Figures 4(a)-4(e) and 5(a)-5(e), respectively. The theoretical predictions for all parameters are plotted with dashed lines and a (*) symbol while the results obtained from analyzing FORTE data are plotted with solid lines and a (+) symbol. We note that only a single peak electron density can be deduced from the fit of the time delay ratio given by

Eq. 16. This value corresponds to the electron density at zenith and should therefore be compared with the theoretical predictions at the maximum elevation angle.

Case 1 shows the best agreement between the ionospheric parameters deduced from the FORTE data and the predictions of IRI, GEOMAG, and ITF. The discrepancies maximize in the tens of percent. Considering that the absolute predictions of IRI in the absence of normalizing data can be off by factors of two, the agreement for Case 1 is remarkable. Case 2 clearly illustrates the variation in absolute accuracy to be expected from ionospheric models such as IRI with differences approaching a factor of two or more. On the other hand the magnetic term is reproduced in all three cases to less than 25 % except for three points associated with case 2. Overall, Case 3 is intermediate in agreement to Cases 1 and 2. We emphasize that these results should not be interpreted as a statement regarding the precision of the geomagnetic model. Rather they reflect the accuracy to which we can extract the density weighted longitudinal component of the geomagnetic field from the ITF/IRI model for ionospheric dispersion.

While this comparison suggests that broadband VHF data such as the FORTE measurements can be used to extract relevant ionospheric parameters, the accuracy of such an analysis can only be determined by comparison to actual measurements such as might be available from ionosondes. To this end we searched the data-base of the World Data Center for ionosonde measurements of the peak electron density or corresponding F2 layer O-mode (ordinary) critical frequency (fof2). The two closest stations to Los Alamos are located at White Sands, NM and Boulder, Colorado. Generally, these stations collect ionosonde data on an hourly basis throughout the year; however, no data was compiled for 1998. In fact we were only able to obtain relevant data in the 1995-

1997 time frame from the Boulder station for Cases 1 and 3. An average over the three years of the peak electron density at the appropriate time of day and day of the year for Case 1 was found to be $3.88 \times 10^{11} \text{ (m}^{-3}\text{)}$ compared to the value of $5.23 \times 10^{11} \text{ (m}^{-3}\text{)}$ deduced from the FORTE data. For case 2 the corresponding values are $2.57 \times 10^{11} \text{ (m}^{-3}\text{)}$ versus $5.76 \times 10^{11} \text{ (m}^{-3}\text{)}$. While this comparison supports our previous conclusion, it does little to define the accuracy of the FORTE analysis technique. Given the large variability in ionospheric conditions from year to year and with latitude, more relevant ionosonde data for the pulser location at the time of operation would have to be collected in order to arrive at an estimate of the accuracy.

5. CONCLUSIONS

The transfer function for the ionosphere was derived in the limit that the frequencies of interest are much larger than the peak plasma frequency of the ionosphere (i.e., $X = \omega_{pe}^2 / \omega^2 \ll 1$) and for a radial electron density profile. Expressions are provided for the phase and time delay corrections introduced by the ionosphere to second order in X assuming that the electromagnetic wave is constrained to reach the receiver. The results contain correction terms that are proportional to the total electron content or TEC along the slant path, to the integrated product of the electron density and the longitudinal gyrofrequency along the slant path, and to higher order integral moments of the electron density. In addition, there is a term that results from refractive bending effects and that depends on the elevation angle of the receiver. By fitting FORTE measurements of the Los Alamos Portable Pulser to a polynomial in $1/\omega$ and as a function of elevation angle, it

is possible to extract the slant TEC, the longitudinal magnetic field strength, the peak electron density, and an effective slant thickness for the ionosphere. The accuracy of this technique could not be checked without ionosonde measurements for the appropriate location and local time. However, a comparison with the Los Alamos Ionospheric Transfer Code (ITF) which uses the International Reference Ionosphere to generate the electron density profile and the United States Geological Survey geomagnetic field model to obtain the magnetic field magnitude and orientation yields agreement to within the factor of two absolute accuracy expected for predicting ionospheric effects from these combined models. We conclude that broadband VHF measurements of transionospheric impulsive signals can be exploited to obtain important information about the Earth's ionosphere along the slant path from source to receiver with the technique described in this article. A constellation of such receivers together with strategically placed impulsive transmitters over the surface of the earth could be used to monitor the ionosphere on a global scale.

ACKNOWLEDGEMENTS

The work described here was performed under the auspices of the United States Department of Energy. We are indebted to the FORTE operations team, led by Phil Klingner and Diane Roussel-Dupré, for constant support in acquiring and working with FORTE data. We are also indebted to David Smith and Daniel Holden for operation of the LAPP facility.

REFERENCES

Bilitza , D. (ed.), International Reference Ionosphere 1990, *NSSDC 90-22*, Greenbelt, Maryland, 1990.

Bilitza, D., K. Rawer, L. Bossy, and T. Gulyaeva, International Reference Ionosphere - Past, Present, Future, *Adv. Space Res.* **13**, No. 3, 3-23, 1993.

Budden, K.G., The Propagation of radio waves: the theory of radio waves of low power in the ionosphere and magnetosphere, *Cambridge University Press, New York*, pp. 1-669, 1985.

Davies, K., Ionospheric Radio Propagation, *National Bureau of Standards Monograph 80*, US Government Printing Office, Washington DC, pp. 1-470, 1965.

Holden, D.N., C.P. Munson, and J.C. Devenport, Satellite observations of transionospheric pulse pairs, *Geophys. Res. Lett.* **22**, 889, 1995.

Jacobson, A.R., K.L. Cummins, M. Carter, P. Klingner, D. Roussel-Dupré, and S.O. Knox, FORTE radio-frequency observations of lightning strokes detected by the National Lightning Detection Network, *J. Geophys. Res.* **105**, No. D12, 15,653, 2000.

Jacobson, A.R., S.O. Knox, R. Franz, and D.C. Enemark, FORTE observations of lightning radio-frequency signatures: Capabilities and basic results, *Radio Sci.* **34**, No. 2, 337-354, 1999.

Kelley M.C., The Earth's Ionosphere: Plasma Physics and Electrodynamics, *Academic Press, Inc., San Diego, International Geophysics Series 43*, Appendix A, 1989.

Massey, R.S. and D.N. Holden, Phenomenology of transionospheric pulse pairs, *Radio Sci.* **30**, No. 5, 1645, 1995.

Massey, R.S., S.O. Knox, R.C. Franz, D.N. Holden, and C.T. Rhodes, Measurements of transionospheric radio propagation parameters using the FORTE satellite, *Radio Sci.* **33**, No. 6, 1739-1753, 1998.

Quinn, J. M., R. J. Coleman, D L. Shiel, and J. M. Nigro; The Joint US/UK 1995 Epoch World Magnetic Model, *Technical Report NO. 314, Naval Oceanographic Office*, 1995.

Rawer, K. and P.A. Bradley, editors of International Reference Ionosphere--Status 1986/87, *Advances in Spa. Res.*, **7**, No. 6, pp. 1-129, 1987.

Rishbeth, H. and O.K. Garriott., Introduction to Ionospheric Physics, *Academic Press, Inc., New York, International Geophysics Series 14*, pp. 1-331, 1969.

Figure 1: (a) Impulse response of a simplified ionosphere (see text) with a $\text{TEC} = 1 \times 10^{17} \text{ m}^{-2}$, $f_{\text{ce}} = 0.8 \text{ MHz}$, $\theta = 20^\circ$, and $t_0 = 1 \mu\text{s}$.

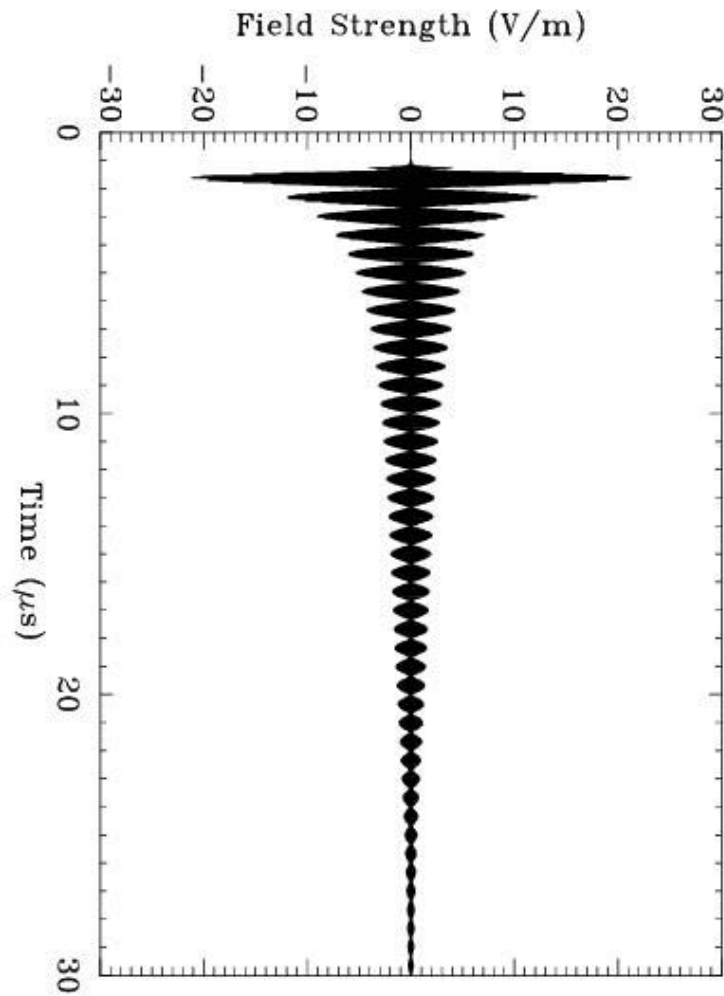


Figure 1: (b) The corresponding spectrogram for the impulse response of the ionosphere shown in (a).

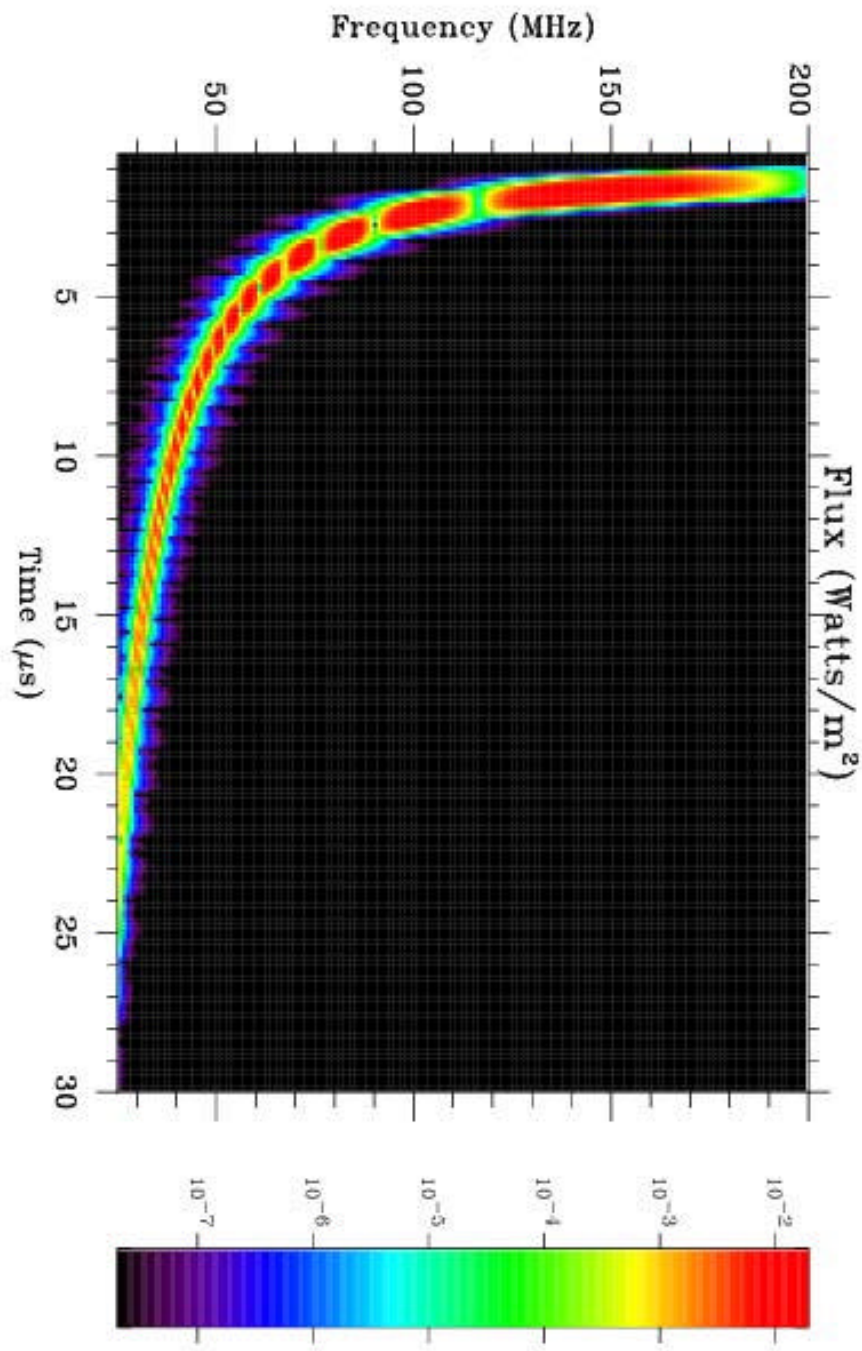


Figure 2: (a) Logarithm of the carrier-suppressed, un-dispersed spectrogram for part of the low band. (b) Corresponding simultaneous spectrogram for the entirety of the high band, after carrier suppression. The color scale extends over 70 dB of total range. The dispersion removal has used a value of $8.54 \times 10^{17} \text{ m}^{-2}$ for the slant total electron content. (c) Low-band median curve (as 40 black triangles) and the high-band cursor points (as 10 black triangles). The data and fitted points in are already un-dechirped in the same manner as are the spectrograms. The blue squares are a coordinated fit of true slant TEC and the quartic effect, *using only the 40 low-band median points*. The red squares are also a coordinated fit of true slant TEC and the quartic effect, *but using both the 40 low-band median points and the high-band cursor points*. The red points are fit with a true slant TEC of $5.31 \times 10^{17} \text{ m}^{-2}$ coordinated with a quartic delay at 100 MHz of $0.43 \mu\text{s}$. The blue points, ignoring the upper band, give a true slant TEC of $4.18 \times 10^{17} \text{ m}^{-2}$ coordinated with a quartic delay at 100 MHz of $0.53 \mu\text{s}$.

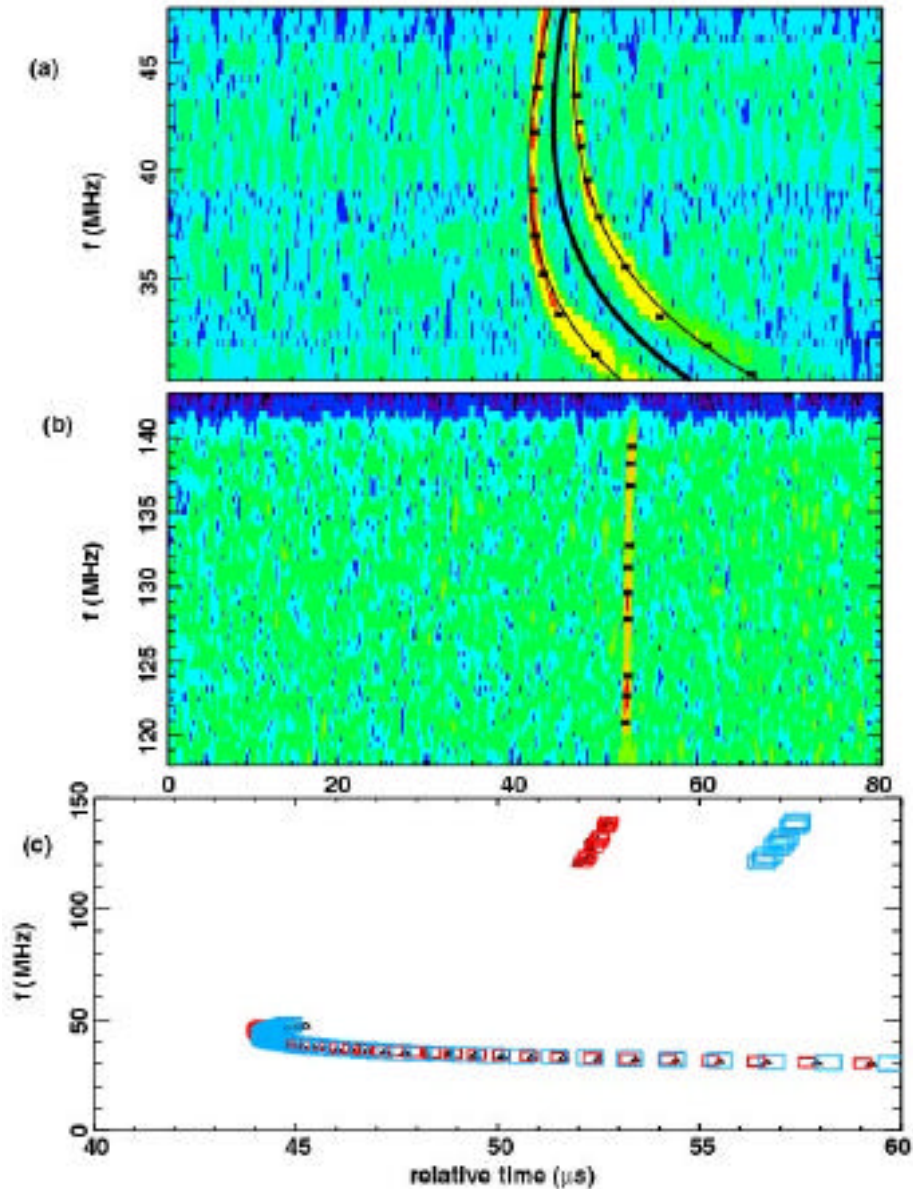
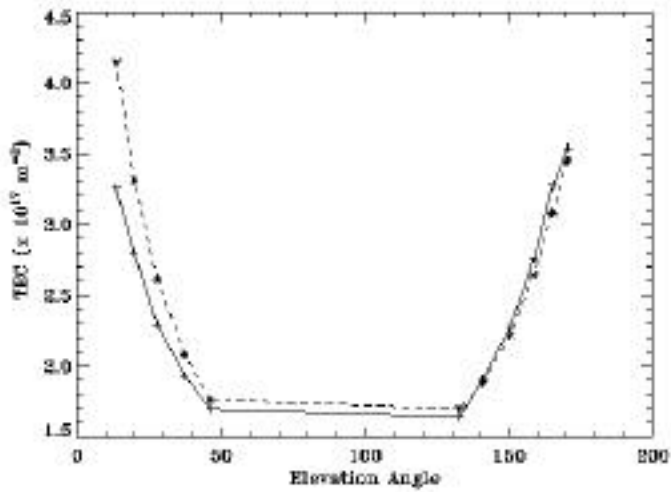


Figure 3: Theoretical predictions (dashed lines with * symbols) for ionospheric parameters obtained with ITF vs. the corresponding parameters (solid lines with + symbols) deduced from the FORTE measurements of the LAPP pulse as a function of elevation angle for Case 1. (a) TEC, (b) quartic time delay at 100 MHz, (c) peak electron density, (d) effective slant thickness of the ionosphere, and (e) the longitudinal component of the electron gyrofrequency. (page 33)

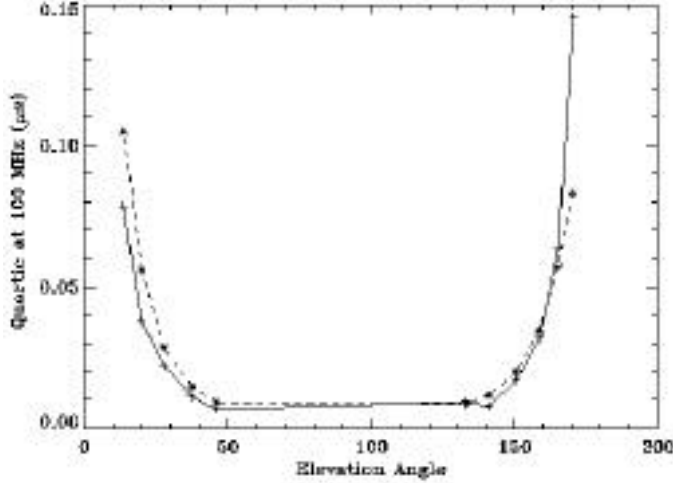
Figure 4: Theoretical predictions (dashed lines with * symbols) for ionospheric parameters obtained with ITF vs. the corresponding parameters (solid lines with + symbols) deduced from the FORTE measurements of the LAPP pulse as a function of elevation angle for Case 2. (a) TEC, (b) quartic time delay at 100 MHz, (c) peak electron density, (d) effective slant thickness of the ionosphere, and (e) the longitudinal component of the electron gyrofrequency. (page 34)

Figure 5: Theoretical predictions (dashed lines with * symbols) for ionospheric parameters obtained with ITF vs. the corresponding parameters (solid lines with + symbols) deduced from the FORTE measurements of the LAPP pulse as a function of elevation angle for Case 3. (a) TEC, (b) quartic time delay at 100 MHz, (c) peak electron density, (d) effective slant thickness of the ionosphere, and (e) the longitudinal component of the electron gyrofrequency. (page 35)

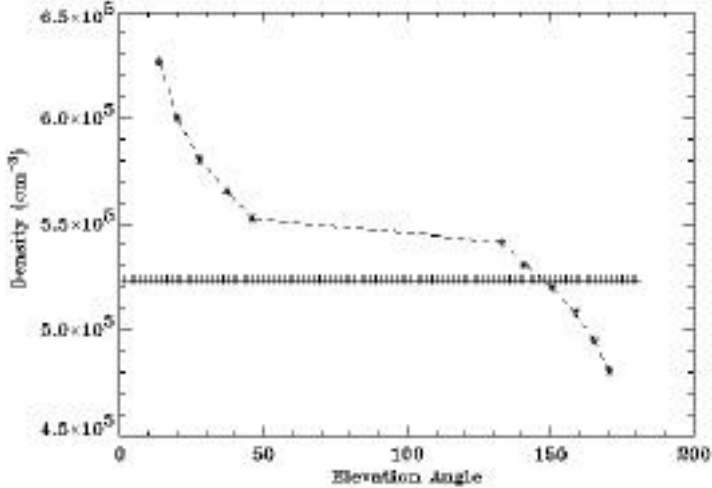
a)



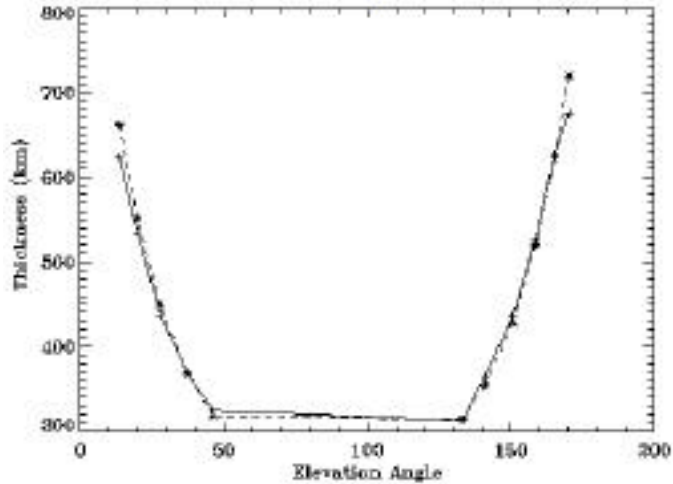
b)



c)



d)



e)

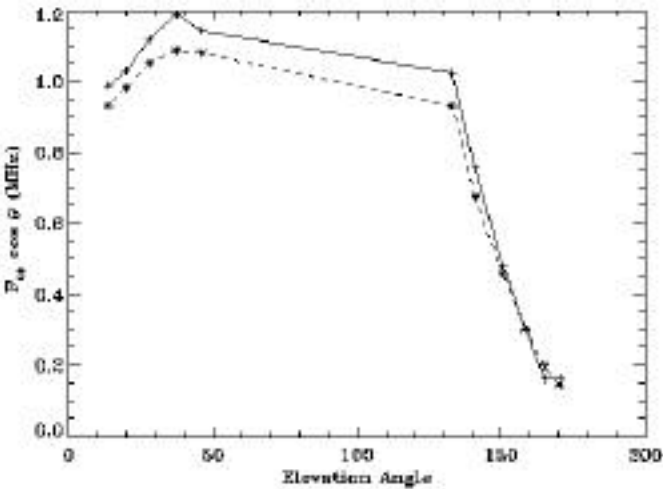
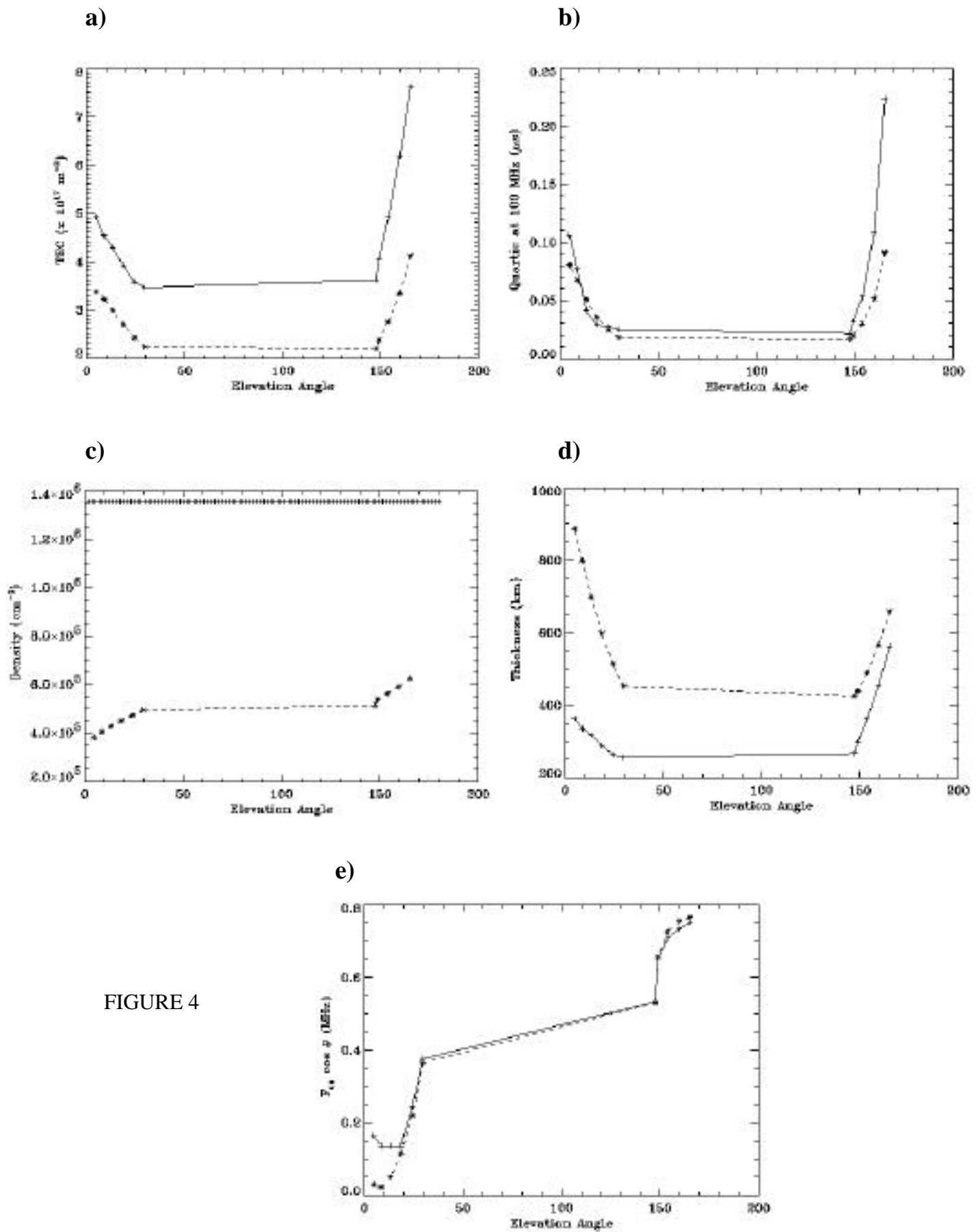
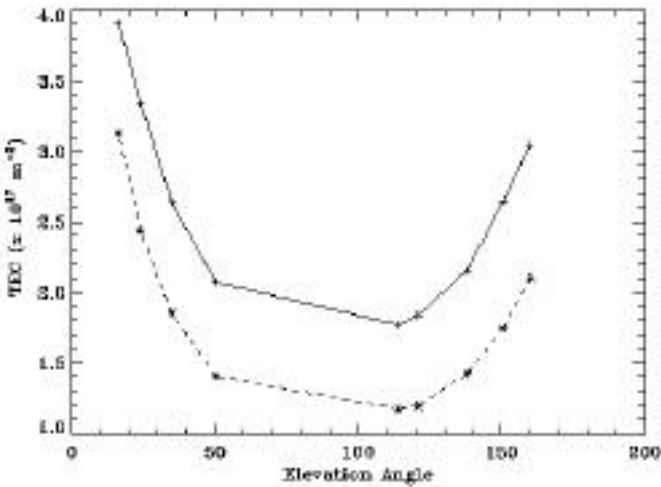


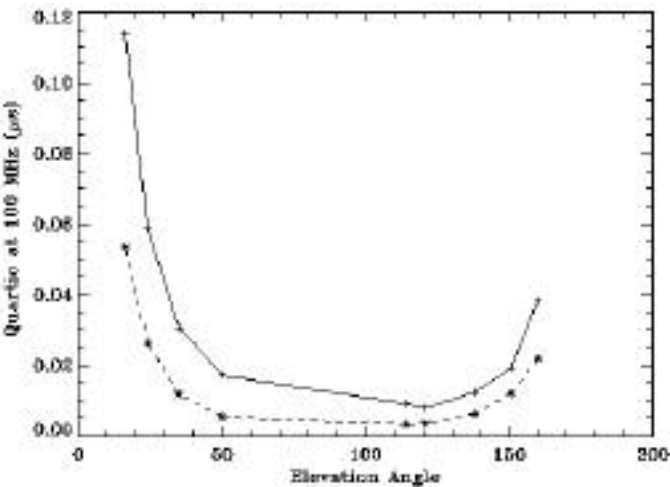
FIGURE 3



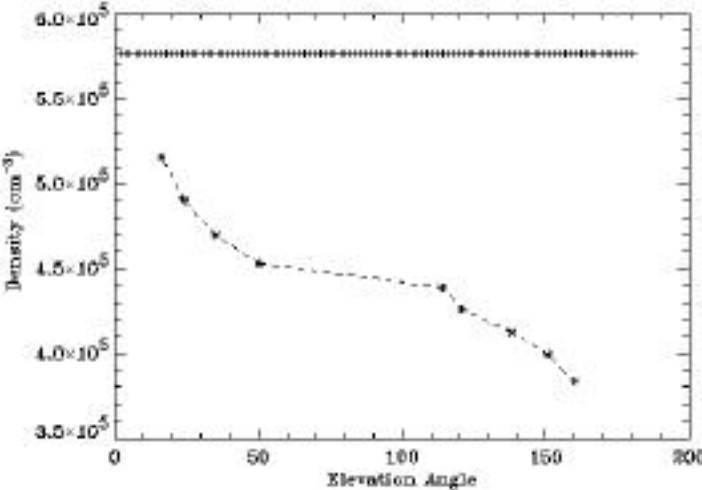
a)



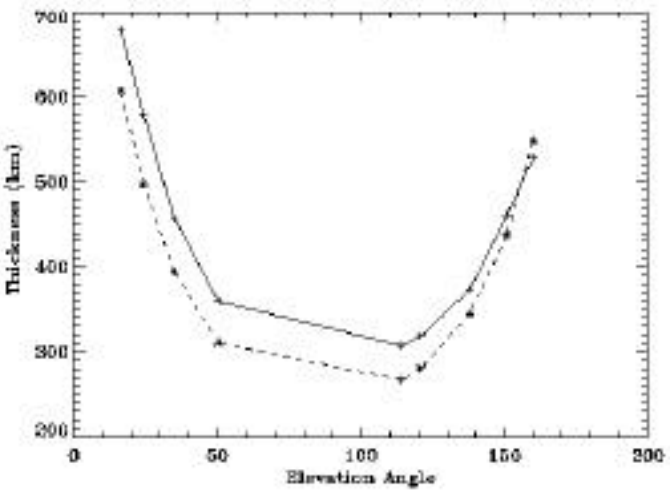
b)



c)



d)



e)

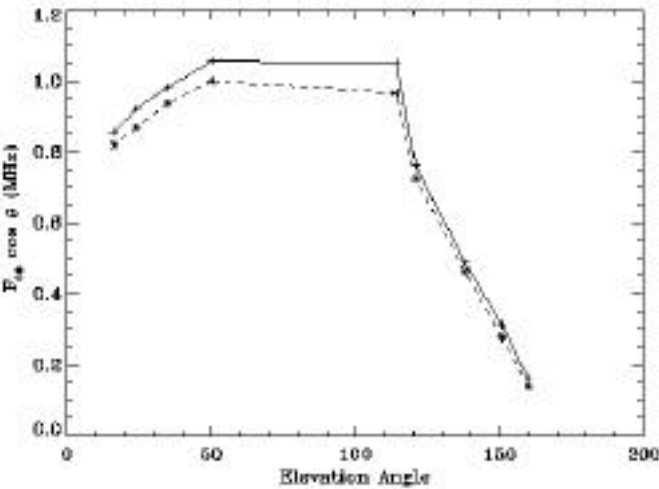


FIGURE 5

Table 1a. FORTE satellite location for eleven collects of the LAPP pulser in the high (118-143 MHz) and 25 February 1998 UT.

Case 1	1	2	3	4	5	6	7	8
UT (month/day/year)	02/25/98	02/25/98	02/25/98	02/25/98	02/25/98	02/25/98	02/25/98	02/25/98
UT Time (hh/mm/ss)	23:29:00	23:30:00	23:31:00	23:32:00	23:33:00	23:34:00	23:35:00	23:36:00
Elevation Angle ($^{\circ}$)	9.55	14.85	21.37	29.54	39.19	47.09	46.18	37.45
Latitude (N)	50.95	47.93	44.86	41.73	38.55	35.34	32.10	28.84
Longitude (E)	-123.94	-121.33	-119.04	-117.01	-115.19	-113.54	-112.04	-110.66
Height (km)	841	839	838	837	835	834	832	831

Table 1b. FORTE satellite location for eleven collects of the LAPP pulser in the high (118-143 MHz) and low (143-175 MHz) bands on 12 September 1998 UT.

Case 2	1	2	3	4	5	6	7	8
UT (month/day/year)	09/12/98	09/12/98	09/12/98	09/12/98	09/12/98	09/12/98	09/12/98	09/12/98
UT Time (hh/mm/ss)	19:08:00	19:09:00	19:10:00	19:11:00	19:12:00	19:13:00	19:14:00	19:15:00
Elevation Angle (°)	14.75	20.33	26.22	31.10	32.57	29.67	24.27	18.49
Latitude (N)	27.47	30.77	34.05	37.30	40.51	43.68	46.80	49.87
Longitude (E)	-122.34	-120.99	-119.53	-117.93	-116.16	-114.20	-111.99	-109.49
Height (km)	804	805	806	807	808	810	811	813

Table 1c. FORTE satellite location for nine collects of the LAPP pulser in the high (118-143 MHz) and 1 June 1998 UT.

Case 3	1	2	3	4	5	6	7
UT (month/day/year)	06/03/98	06/03/98	06/03/98	06/03/98	06/03/98	06/03/98	06/03/98
UT Time (hh/mm/ss)	01:53:00	01:54:00	01:55:00	01:56:00	01:57:00	01:58:00	01:59:00
Elevation Angle (°)	20.18	29.26	42.15	59.13	65.94	50.38	35.02
Latitude (N)	48.79	45.70	42.55	39.36	36.13	32.87	29.59
Longitude (E)	-110.94	-108.55	-106.44	-104.54	-102.84	-101.29	-99.87
Height (km)	808	807	806	805	804	803	803